Geometric Decomposition of Eddy Feedbacks in Barotropic Systems

STEPHANIE WATERMAN

Department of Earth, Ocean and Atmospheric Sciences, University of British Columbia, Vancouver, British Columbia, Canada, and Climate Change Research Centre and ARC Centre of Excellence for Climate System Science, University of New South Wales, Sydney, New South Wales, Australia

JONATHAN M. LILLY

NorthWest Research Associates, Redmond, Washington

(Manuscript received 26 August 2014, in final form 1 January 2015)

ABSTRACT

In oceanic and atmospheric flows, the eddy vorticity flux divergence—denoted "F" herein—emerges as a key dynamical quantity, capturing the average effect of fluctuations on the time-mean circulation. For a barotropic system, F is derived from the horizontal velocity covariance matrix, which itself can be represented geometrically in terms of the so-called variance ellipse. This study proves that F may be decomposed into two different components, with distinct geometric interpretations. The first arises from variations in variance ellipse orientation, and the second arises from variations in the kinetic energy of the anisotropic part of the velocity fluctuations, which can be seen as a function of variance ellipse size and shape. Application of the divergence theorem shows that F integrated over a closed region is explained entirely by separate variations in these two quantities around the region periphery. A further decomposition into four terms shows that only four specific spatial patterns of ellipse variability can give rise to a nonzero eddy vorticity flux divergence. The geometric decomposition offers a new tool for the study of eddy–mean flow interactions, as is illustrated with application to an unstable eastward jet on a beta plane.

1. Introduction

The turbulent ocean and atmosphere are full of rapidly evolving perturbations, or "eddies," superposed on a more slowly evolving mean or background state. In many situations, eddies have important feedbacks on the mean state that cannot be neglected in the description of the mean dynamics. As a consequence we seek ways to know and understand these eddy–mean flow interactions, both because this knowledge is a necessary ingredient of understanding the dynamics of the atmospheric and oceanic circulations and because it promises guidance in correctly parameterizing the net effects of unresolved eddies in numerical models.

A traditional approach to the study of these interactions is to decompose key dynamical quantities into a "mean," or time-invariant, portion and an eddy, or fluctuating, portion. This so-called Reynolds decomposition leads to equations for a time-mean field being forced by the time mean of an eddy flux divergence. Eddy–mean flow feedbacks can then be studied by understanding the patterns of time-mean eddy flux divergences of vorticity or other dynamical quantities, why they arise, and the effect they have on the time-mean quantities. There is a long and detailed history of work that aims to achieve these goals, both in studies of the atmospheric and oceanic circulations and using observations as well as model output (e.g., Hoskins 1983; Plumb 1986; Holland and Rhines 1980; Marshall 1984; Cronin 1996; Gent and McWilliams 1996; Young 2012).

In parallel with such dynamical studies, another approach aims for a more descriptive characterization of flow variability, and here variance ellipses are a common tool. Variance ellipses (see, e.g., Preisendorfer 1988) capture the essential geometric features of the fluctuating horizontal velocity field, encoding information about eddy kinetic energy, anisotropy, and orientation.

Corresponding author address: Stephanie Waterman, Department of Earth, Ocean and Atmospheric Sciences, University of British Columbia, Room 2020, Earth Sciences Building, 2207 Main Mall, Vancouver, BC V6T 1Z4, Canada.
E-mail: snw@alum.mit.edu

DOI: 10.1175/JPO-D-14-0177.1

It is known that variance ellipses have a close relationship to the eddy horizontal momentum flux. As such they have been used by many investigators (e.g., Morrow et al. 1994; Ohlmann and Niiler 2005; Scott et al. 2008; Trani et al. 2011; Lumpkin and Johnson 2013) to describe both the time-mean properties of the eddy motion as well as the eddy forcing of the mean flow.

This paper unifies these dynamical and descriptive approaches to analyzing eddy variability for barotropic, quasigeostrophic dynamics. It is shown that the eddy forcing in the form of the eddy vorticity flux divergence can be decomposed into two terms with distinct geometric interpretations: one arising from variations in the anisotropy of the variance ellipses and the second arising from variations in the ellipse orientation. The decomposition method is illustrated with an application to a simple model of an eastward, unstable, barotropic jet on a beta plane, an idealized representation of western boundary current jet systems (Waterman et al. 2011; Waterman and Jayne 2011; Waterman and Hoskins 2013).

The geometric decomposition developed here offers a new tool for the study of eddy–mean flow interactions, with the potential to (i) identify the important ingredients of the eddy variability that have a mean flow forcing effect; (ii) offer a simplified description of the origin of eddy–mean flow feedbacks in terms of the spatial patterns of variance ellipse geometry; and (iii) suggest a conceptual picture of the mechanisms of eddy–mean flow interactions. It is also relevant to parameterization efforts, as it extends the parameterization framework recently introduced by Marshall et al. (2012) by adding new insight into the geometric origin of eddy–mean flow feedbacks.

2. Background

The structure of the fluctuating, or eddy, portion of the horizontal velocity field is described by the velocity covariance matrix:

$$\mathbf{C} \equiv \begin{bmatrix} \langle u'u' \rangle & \langle u'v' \rangle \\ \langle u'v' \rangle & \langle v'v' \rangle \end{bmatrix}, \tag{1}$$

where the angled braces represent a temporal average, and the primes denote departures from that average, that is, $u' \equiv u - \langle u \rangle$ and $v' \equiv v - \langle v \rangle$. Here, u and v are the eastward and northward velocity components, respectively. The covariance matrix—also known as the eddy momentum flux tensor or eddy stress tensor—has both a geometric as well as a dynamical significance. We address both of these in turn before showing how these two perspectives may be unified.

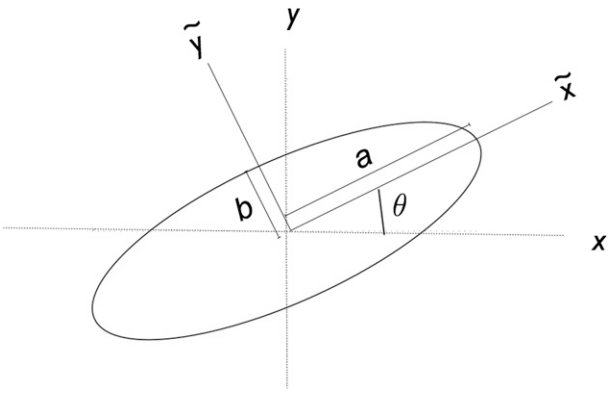

FIG. 1. Definitions of the variance ellipse geometry parameters and a rotated $(\tilde{x}, \tilde{y})$ coordinate system aligned with the ellipse orientation.

a. Geometric interpretation

The covariance matrix defines an ellipse, known as the variance ellipse. The eigenvalue decomposition of $\mathbf{C}$ can be written as

$$\mathbf{C} = \begin{bmatrix} \cos\theta & -\sin\theta \\ \sin\theta & \cos\theta \end{bmatrix} \begin{bmatrix} a^2 & \\ & b^2 \end{bmatrix} \begin{bmatrix} \cos\theta & -\sin\theta \\ \sin\theta & \cos\theta \end{bmatrix}^{\mathrm{T}}, \tag{2}$$

with a being the semimajor axis length, b being the semiminor axis length, and θ being the inclination of the major axis counterclockwise from the x axis; here, the superscript T denotes the matrix transpose. The ellipse parameters a, b, and θ are illustrated in the schematic in Fig. 1.

The eigenvalue decomposition of $\mathbf{C}$ may be rewritten as the sum of an isotropic portion and an anisotropic portion. With $\mathbf{I}$ being the identity matrix, an alternative yet equivalent expression for $\mathbf{C}$ is

$$\mathbf{C} = K\mathbf{I} + L \begin{bmatrix} \cos 2\theta & \sin 2\theta \\ \sin 2\theta & -\cos 2\theta \end{bmatrix}, \tag{3}$$

where $K = (a^2 + b^2)/2$ is the eddy kinetic energy, and $L = (a^2 - b^2)/2$ is the excess kinetic energy of velocity fluctuations in the major axis direction compared with the minor axis direction. The term L is therefore a measure of the kinetic energy associated with the anisotropic, or "polarized," portion of the velocity fluctuations; this parameter will be referred to simply as the ellipse anisotropy. Note that only L, and not K, appears in terms that depend on the orientation θ. Since $L/K = (a^2 - b^2)/(a^2 + b^2)$ is a measure of ellipse shape varying like the eccentricity between zero and one, we see that the ellipse anisotropy L combines

information about the ellipse size together with ellipse shape.[1]

In (3) we can readily see how the ellipse parameters K, L, and θ are related to the velocity covariance terms in the components of $\mathbf{C}$. One finds that

$$K = \frac{1}{2}(a^2 + b^2) = \frac{1}{2}\langle u'^2 + v'^2 \rangle, \tag{4}$$

$$L = \frac{1}{2}(a^2 - b^2) = \frac{1}{2}\sqrt{\langle u'u' - v'v' \rangle^2 + 4\langle u'v' \rangle^2}, \quad \text{and} \tag{5}$$

$$\theta = \frac{1}{2}\arctan\left(\frac{2\langle u'v' \rangle}{\langle u'u' - v'v' \rangle}\right), \tag{6}$$

with expressions for a^2 and b^2 following at once by adding and subtracting the top two equations.

b. Dynamical interpretation

The covariance matrix can be related to eddy fluxes and thus to the eddy forcing of the mean flow. For the barotropic, quasigeostrophic flow we consider here, the eddy forcing of the time-mean vorticity equation is given by the time-mean eddy vorticity flux divergence:

$$F \equiv \nabla \cdot \langle \mathbf{u}'\zeta' \rangle, \tag{7}$$

which for brevity will simply be referred to as the "eddy forcing." Here, $\zeta \equiv v_x - u_y$ (where subscripts denote partial derivatives in the direction specified) is the vertical component of the relative vorticity, and $\zeta' \equiv \zeta - \langle \zeta \rangle$ is its fluctuating part.

It is well known that F can be equivalently expressed as the curl of the divergence of the velocity covariance matrix:

$$F = \mathbf{k} \cdot [\nabla \times (\nabla \cdot \mathbf{C})], \tag{8}$$

where $\mathbf{k}$ is the vertical unit vector.[2] Following Hoskins et al. (1983), we write the velocity covariance matrix as

$$\mathbf{C} = K\mathbf{I} + \begin{bmatrix} M & N \\ N & -M \end{bmatrix}, \tag{9}$$

with $M \equiv (\langle u'^2 - v'^2 \rangle)/2$ and $N \equiv \langle u'v' \rangle$. In this notation, the eddy forcing F becomes

$$F = -2M_{xy} + N_{xx} - N_{yy}, \tag{10}$$

where the subscripts denote partial derivatives. This shows that F depends on second partial derivatives of the terms in the anisotropic portion of $\mathbf{C}$. Note that the kinetic energy itself does not appear in this expression.

[1] Note that L/K is equivalent to $\gamma_m K$ in the notation of Marshall et al. (2012) or $\hat{M}$ in the notation of Hoskins et al. (1983).

[2] In this expression, $\mathbf{C}$ is interpreted as a 3×3 matrix with zeros in the final row and final column.

3. A geometric decomposition of the eddy forcing

For presentational clarity, we will first state the main results without proof. The derivations will be given subsequently in section 3b.

a. Main results

The first main result of this paper is to recognize that the eddy forcing F can be decomposed into two distinct portions:

$$F = F_\theta + F_L = \nabla \cdot \mathbf{f}_\theta + \nabla \cdot \mathbf{f}_L, \tag{11}$$

where the vector $\mathbf{f}_\theta$ depends only on spatial changes in the ellipse orientation θ, while $\mathbf{f}_L$ depends only on spatial changes in the ellipse anisotropy L. The vectors $\mathbf{f}_\theta$ and $\mathbf{f}_L$ can be expressed as matrix multiplications of the horizontal gradients of θ and L as

$$\mathbf{f}_\theta = \begin{bmatrix} \cos 2\theta & \sin 2\theta \\ \sin 2\theta & -\cos 2\theta \end{bmatrix} 2L\nabla\theta, \quad \text{and} \tag{12}$$

$$\mathbf{f}_L = \begin{bmatrix} \sin 2\theta & -\cos 2\theta \\ -\cos 2\theta & -\sin 2\theta \end{bmatrix} \nabla L, \tag{13}$$

with the gradient vectors $\nabla\theta$ and ∇L being regarded as 2-vectors in these expressions.

It can be shown that the vector $\mathbf{f} = \mathbf{f}_\theta + \mathbf{f}_L$ is the divergent part of the eddy vorticity flux vector $\langle \mathbf{u}'\zeta' \rangle$. These two differ by a nondivergent vector, say $\mathbf{g}$, such that the divergences of $\mathbf{f}$ and $\langle \mathbf{u}'\zeta' \rangle$ are the same, $\nabla \cdot \mathbf{f} = \nabla \cdot \langle \mathbf{u}'\zeta' \rangle$, even though $\mathbf{f}$ and $\langle \mathbf{u}'\zeta' \rangle$ are not themselves identical.

The proof that substituting (12) and (13) into (11) does indeed recover F as expressed by (10) is straightforward and is given shortly. We note that the matrix depending on θ appearing in (12) also occurs in (3). A physical interpretation of this matrix can be established: as will be shown, the action of this matrix is to reflect a vector about the major axis of the variance ellipse. Similarly the matrix in (13) reflects a vector about an axis oriented at 45° between the ellipse major and minor axes.

We can now apply the divergence theorem to find that the integral of F over some area A is given by

$$\int_A F \, dA = \oint_C \mathbf{f}_\theta \cdot \hat{\mathbf{n}} \, ds + \oint_C \mathbf{f}_L \cdot \hat{\mathbf{n}} \, ds, \tag{14}$$

where C is the curve bounding A, $\hat{\mathbf{n}}$ is the outward unit normal vector, and ds is a differential element of arc length. Thus, because of the divergence theorem combined with (11), any spatial average of F can be decomposed into two portions: one of which depends only on variations of the ellipse orientation θ around the region boundary and a second that depends only on variations of the anisotropy L around the boundary.

To find expressions for $F_\theta \equiv \nabla \cdot \mathbf{f}_\theta$ and $F_L \equiv \nabla \cdot \mathbf{f}_L$, we note, by comparing (3) and (9), that $M = L\cos 2\theta$ and $N = L\sin 2\theta$. Inserting these into the expression for F given by (10) leads to

$$F = -2\frac{\partial^2}{\partial x \partial y}(L\cos 2\theta) + \left(\frac{\partial^2}{\partial x^2} - \frac{\partial^2}{\partial y^2}\right)(L\sin 2\theta), \qquad (15)$$

and, carrying out the indicated differentiation, we obtain an explicit expression for F in terms of variations of L and θ. The resulting expression is somewhat complicated on account of the cosine and sine terms but is conveniently presented in a rotated coordinate system that is aligned with the local orientation of the variance ellipse at the current point (see Fig. 1); the more general expression will be presented later.

In this local ellipse frame, with $\tilde{x}$ oriented along the major axis of the ellipse and $\tilde{y}$ oriented along the minor axis, F can be written as

$$F = \overbrace{-2\frac{\partial^2 L}{\partial \tilde{x}\partial \tilde{y}}}^{F_1} + \overbrace{4\left(\frac{\partial L}{\partial \tilde{x}}\frac{\partial \theta}{\partial \tilde{x}} - \frac{\partial \tilde{L}}{\partial \tilde{y}}\frac{\partial \theta}{\partial \tilde{y}}\right)}^{F_2} + \overbrace{2L\left(\frac{\partial^2 \theta}{\partial \tilde{x}^2} - \frac{\partial^2 \theta}{\partial \tilde{y}^2}\right)}^{F_3} + \overbrace{8L\frac{\partial \theta}{\partial \tilde{x}}\frac{\partial \theta}{\partial \tilde{y}}}^{F_4}, \qquad (16)$$

and this four-term decomposition accounts for our second main result. As will be shown shortly, these four terms combine to give the two-term decomposition in terms of F_θ and F_L as

$$F_L = F_1 + \frac{1}{2}F_2, \quad F_\theta = \frac{1}{2}F_2 + F_3 + F_4, \qquad (17)$$

where we note that F_2 contributes to both quantities. These four terms arise naturally in the course of deriving the two-term decomposition. However, it is not clear from the application to the jet system presented later whether the four-term decomposition forms a useful analysis tool in its own right or is simply a mathematical truth that helps us understand the contributions to the two-term decomposition. The latter is ultimately more powerful as it gives us access to spatial integration via the divergence theorem, yet the former has a compelling geometric interpretation, as we show next.

A schematic illustrating the spatial patterns of ellipse geometry that give rise to contributions from each of these four terms F_1–F_4 is presented in Fig. 2. The term F_1 corresponds to a bilinear rate of change of the anisotropy L in both the major and minor axis directions; F_2 is a cross term arising from the difference of the product of gradients of the anisotropy and the orientation between the major axis and minor axis directions; F_3 is the difference in curvature of the orientation angle between the major and minor axis directions; and F_4 arises from a simultaneous gradient of the orientation angle in both the major and minor axis directions. Perhaps a more intuitive explanation of these terms is that they result from generalizations of the Laplacian (in the case of F_1 and F_3) or of an inner product between two vectors (in the case of F_2 and F_4) that are modified to incorporate a reflection operation; this will become apparent in the next subsection.

The four-term decomposition is important because it identifies the only possible patterns of variance ellipse distributions that can give rise to an eddy forcing. In the appendix, we ask how many possible second-order spatial rates of change exist. We find that there are 9 second-order horizontal derivatives of K, L, and θ and 21 possible squares of first-order horizontal derivatives for a total of 30 second-order terms. Of these, only four—two second-order derivatives and two products of first-order derivatives—appear in the eddy forcing. This implies that most of the structure we observe in the distribution of variance ellipses over a flow field is irrelevant as far as eddy–mean flow forcing is concerned. One may see this point as clarifying the nature of the second-order partial derivatives occurring in the definition of F in (8) or its expression in terms of the elements of the covariance matrix in (10). These derivatives introduce a certain "gauge freedom," whereby many aspects of the spatial patterns of the variance ellipses may be changed, without modifying the eddy forcing F.[3] See the appendix for further discussion of the spatial derivatives that do *not* contribute to the eddy forcing.

The above results show that one may consider spatial variations of ellipse anisotropy L and spatial variations of ellipse orientation θ as the two ingredients underpinning eddy forcing. Further they reveal that only certain variations of these patterns are relevant to generating a finite eddy forcing. Descriptions of how different geometric terms contribute to the total eddy forcing may be given by examining the spatial patterns in the four-term decomposition [(16)] of F into F_1–F_4 or in the two-term decomposition [(17)] of F into F_L and F_θ. Alternatively, one may choose strategically designed

[3] We thank an anonymous reviewer for bringing this point to our attention.

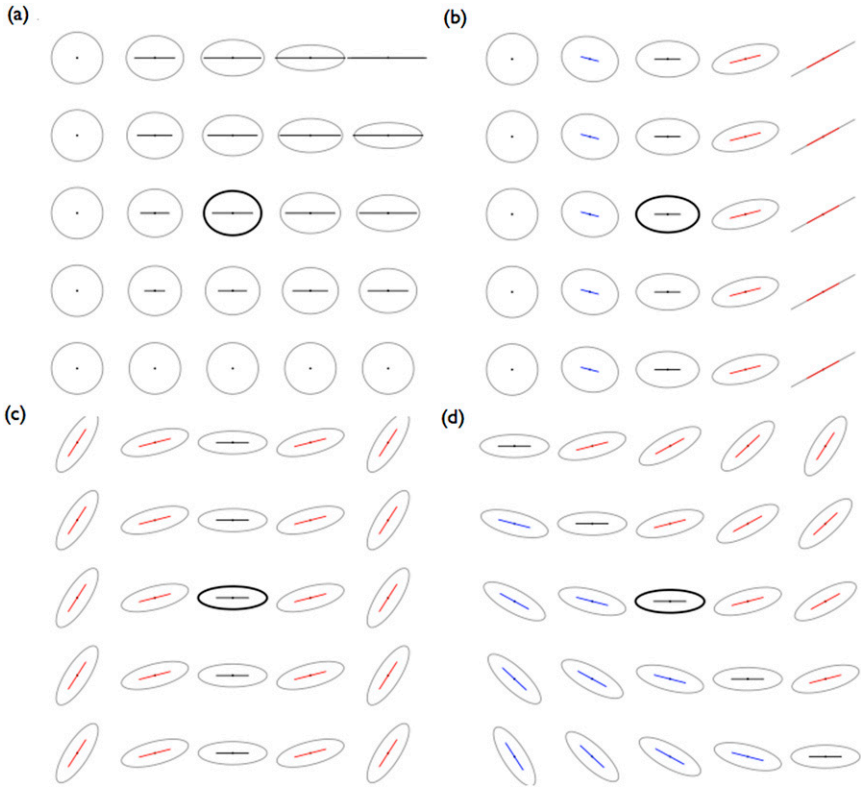

FIG. 2. An illustration of the four spatial patterns of ellipse geometry that contribute to eddy forcing F as described by (16): (a) F_1, (b) F_2, (c) F_3, and (d) F_4. Ellipses are shown in gray, with the central ellipse in each panel drawn with a heavy black line. Directional line segments visualizing the anisotropic portion of the variance ellipses are also shown. Line segments have a length proportional to $\sqrt{L}$ and are shown in red if θ is significantly positive (corresponding to northward tilt with respect to the eastward direction), blue if θ is significantly negative (corresponding to southward tilt with respect to the eastward direction), and black if θ is approximately zero (corresponding to an ellipse/line segment orientation that is east–west or north–south).

regions over which to consider the spatially integrated eddy forcing and then apply the decomposition of the divergence theorem [(14)] of $\mathbf{f}$ into the two terms $\mathbf{f}_\theta$ and $\mathbf{f}_L$ in order to examine the role of L and θ variations around the region boundary.

While the decomposition into the four terms F_1–F_4 given by (16) is conceptually useful in terms of understanding the specific patterns of ellipse geometry that can generate an eddy forcing, in the application to the unstable jet in section 4, F_1–F_4 are found to exhibit a tendency for significant cancellations. These cancellations occur both among the four different terms as well as within the same term in different regions in space. For this reason, the simpler decomposition into just two terms F_θ and F_L, which can be readily averaged in space using the divergence theorem, appears more useful in this example and will be the focus of the application section.

The four-term decomposition has been implemented as a MATLAB function called divgeom, distributed as a part of the freely available toolbox JLAB at the second author's website (www.jmlilly.net). The two-term decomposition can be then found at once through (17). In divgeom, care is taken in the numerical approximation of derivatives. In particular, F_2 and F_3, which both contain products of first-order derivatives, are rewritten as differences of second-order difference terms. Keeping all the derivatives of the same order reduces the numerical error so that the sum of the geometric terms computed separately, $F_1 + F_2 + F_3 + F_4$, more closely matches the eddy vorticity flux divergence F computed directly from (10).

b. *Geometric decomposition of F: Derivation*

Next we derive the results of the previous subsection. Readers not interested in these details may skip directly

to the application in section 4. For convenience we will introduce some new notation. We will make use of the three 2×2 matrices,

$$\mathbf{J}_\theta \equiv \begin{bmatrix} \cos\theta & -\sin\theta \\ \sin\theta & \cos\theta \end{bmatrix}, \quad \mathbf{G} \equiv \begin{bmatrix} 1 & 0 \\ 0 & -1 \end{bmatrix}, \quad \mathbf{H} \equiv \begin{bmatrix} 0 & 1 \\ 1 & 0 \end{bmatrix}, \tag{18}$$

the first of which is the counterclockwise rotation matrix, and the second and third of which are reflection matrices. Also, we use the boldface symbol $\boldsymbol{\nabla}$ to denote the gradient operator regarded as a two-vector:

$$\boldsymbol{\nabla} \equiv \begin{bmatrix} \dfrac{\partial}{\partial x} \\ \dfrac{\partial}{\partial y} \end{bmatrix}, \tag{19}$$

which will enable us to keep more explicit track of differentiations. With this notation, $\boldsymbol{\nabla}^{\mathrm{T}}\mathbf{f}$ is the divergence of a two-vector $\mathbf{f}$, and $(\boldsymbol{\nabla}^{\mathrm{T}}\boldsymbol{\nabla})g$ is the Laplacian of a scalar field g.

1) Derivation of the four-term decomposition

With these definitions, two alternate second-order differential operators in addition to the Laplacian can be defined as

$$\boldsymbol{\nabla}^{\mathrm{T}}\mathbf{G}\boldsymbol{\nabla} = \frac{\partial^2}{\partial x^2} - \frac{\partial^2}{\partial y^2}, \quad \boldsymbol{\nabla}^{\mathrm{T}}\mathbf{H}\boldsymbol{\nabla} = 2\frac{\partial^2}{\partial x \partial y}, \tag{20}$$

and in this notation $F = -2M_{xy} + N_{xx} - N_{yy}$ becomes

$$F = (\boldsymbol{\nabla}^{\mathrm{T}}\mathbf{G}\boldsymbol{\nabla})N - (\boldsymbol{\nabla}^{\mathrm{T}}\mathbf{H}\boldsymbol{\nabla})M. \tag{21}$$

Factoring out the final divergence leads to $F = \boldsymbol{\nabla}^{\mathrm{T}}\mathbf{f}$, where

$$\mathbf{f} \equiv \mathbf{G}\boldsymbol{\nabla}N - \mathbf{H}\boldsymbol{\nabla}M = \begin{bmatrix} N_x - M_y \\ -N_y - M_x \end{bmatrix}, \tag{22}$$

and we now proceed to express $\mathbf{f}$ in terms of the ellipse anisotropy L and the ellipse orientation θ. Note that we could have chosen to add to $\mathbf{f}$ defined in (22) any nondivergent vector $\mathbf{g}$ and still have $F = \boldsymbol{\nabla}^{\mathrm{T}}(\mathbf{f} + \mathbf{g})$; our definition of $\mathbf{f}$ therefore corresponds to the particular choice $\mathbf{g} = 0$.

The horizontal gradients of $M = L\cos 2\theta$ and $N = L\sin 2\theta$ are found to be

$$\boldsymbol{\nabla}M = (\boldsymbol{\nabla}L)\cos 2\theta - 2L(\boldsymbol{\nabla}\theta)\sin 2\theta, \quad \text{and} \tag{23}$$

$$\boldsymbol{\nabla}N = (\boldsymbol{\nabla}L)\sin 2\theta + 2L(\boldsymbol{\nabla}\theta)\cos 2\theta. \tag{24}$$

To simplify these, we introduce two new matrices:

$$\tilde{\mathbf{G}}_\theta \equiv \mathbf{G}\cos 2\theta + \mathbf{H}\sin 2\theta = \begin{bmatrix} \cos 2\theta & \sin 2\theta \\ \sin 2\theta & -\cos 2\theta \end{bmatrix}, \quad \text{and} \tag{25}$$

$$\tilde{\mathbf{H}}_\theta \equiv \mathbf{H}\cos 2\theta - \mathbf{G}\sin 2\theta = \begin{bmatrix} -\sin 2\theta & \cos 2\theta \\ \cos 2\theta & \sin 2\theta \end{bmatrix}, \tag{26}$$

the interpretations of which will be established shortly. Substituting (23) and (24) into (22) leads to

$$\mathbf{f} = \mathbf{G}\boldsymbol{\nabla}N - \mathbf{H}\boldsymbol{\nabla}M = \overbrace{2L\tilde{\mathbf{G}}_\theta\boldsymbol{\nabla}\theta}^{\mathbf{f}_\theta} \; \overbrace{-\tilde{\mathbf{H}}_\theta\boldsymbol{\nabla}L}^{\mathbf{f}_L} \tag{27}$$

after making use of (25) and (26). This defines $\mathbf{f}_\theta$ and $\mathbf{f}_L$, matching the expressions (12) and (13) given above.

From direct calculation, the matrices $\tilde{\mathbf{G}}_\theta$ and $\tilde{\mathbf{H}}_\theta$ may also be written as

$$\tilde{\mathbf{G}}_\theta = \mathbf{G}\cos 2\theta + \mathbf{H}\sin 2\theta = \mathbf{J}_\theta\mathbf{G}\mathbf{J}_\theta^{\mathrm{T}}, \quad \text{and} \tag{28}$$

$$\tilde{\mathbf{H}}_\theta = \mathbf{H}\cos 2\theta - \mathbf{G}\sin 2\theta = \mathbf{J}_\theta\mathbf{H}\mathbf{J}_\theta^{\mathrm{T}}, \tag{29}$$

in which form we may see their physical interpretation more clearly. They are reflections in the reference frame of the ellipse. The multiplication $\tilde{\mathbf{G}}_\theta\mathbf{x}$ rotates a vector $\mathbf{x}$ into the reference frame of the ellipse, reflects it about the major axis, and rotates it back. The action of $\tilde{\mathbf{H}}_\theta$ is similar except that the intermediate reflection is at a line at 45° to the axes of the ellipse.

We now proceed to find expressions for F_1–F_4. From (23) and (24), taking a second partial derivative of M with respect to y gives

$$M_{xy} = L_{xy}\cos 2\theta - 2L\theta_{xy}\sin 2\theta - 2(L_x\theta_y + L_y\theta_x)\sin 2\theta - 4L\theta_x\theta_y\cos 2\theta, \tag{30}$$

while taking a second partial x derivative of N leads to

$$N_{xx} = L_{xx}\sin 2\theta + 2L\theta_{xx}\cos 2\theta + 4L_x\theta_x\cos 2\theta - 4L|\theta_x|^2\sin 2\theta, \tag{31}$$

with a similar expression for N_{yy}. Combining the above, we find F can be written as $F = F_1 + F_2 + F_3 + F_4$, with the four terms F_1–F_4 given by

$$F_1 \equiv -2\cos 2\theta L_{xy} + \sin 2\theta(L_{xx} - L_{yy}), \tag{32}$$

$$F_2 \equiv 4\cos 2\theta(L_x\theta_x - L_y\theta_y) + 4\sin 2\theta(L_x\theta_y + L_y\theta_x), \tag{33}$$

$$F_3 \equiv 2\cos 2\theta L(\theta_{xx} - \theta_{yy}) + 4\sin 2\theta L\theta_{xy}, \quad \text{and} \tag{34}$$

$$F_4 \equiv 8\cos 2\theta L\theta_x\theta_y - 4\sin 2\theta L(|\theta_x|^2 - |\theta_y|^2). \tag{35}$$

These are the forms we would use in calculating these quantities in a standard (geographic) coordinate frame. However, if we locally choose a coordinate system oriented with the variance ellipse, then all the cosine terms become unity, the sine terms vanish, and we obtain the simplified expression of (16).

2) Derivation of the two-term decomposition

The derivation of the two-term decomposition $F = F_L + F_\theta$ requires keeping careful track of which terms originate from variations in L and which from variations in θ. First, we note that for some matrix $\mathbf{A}$ and some scalar f, one has

$$\nabla^{\mathrm{T}}(\mathbf{A}\nabla f) = (\nabla^{\mathrm{T}}\mathbf{A})\nabla f + \mathrm{tr}(\mathbf{A}^{\mathrm{T}}\nabla\nabla^{\mathrm{T}})f, \tag{36}$$

where tr indicates the matrix trace. Then $F = \nabla^{\mathrm{T}}\mathbf{f}$ becomes

$$F = 2(\nabla L)^{\mathrm{T}}\tilde{\mathbf{G}}_\theta\nabla\theta + 2L(\nabla^{\mathrm{T}}\tilde{\mathbf{G}}_\theta)\nabla\theta + 2L\mathrm{tr}(\tilde{\mathbf{G}}_\theta\nabla\nabla^{\mathrm{T}}\theta) - (\nabla^{\mathrm{T}}\tilde{\mathbf{H}}_\theta)\nabla L - \mathrm{tr}(\tilde{\mathbf{H}}_\theta\nabla\nabla^{\mathrm{T}}L), \tag{37}$$

after substituting $\mathbf{f}$ given by (27) into (36). The first three terms originate from the expansion of $2L\tilde{\mathbf{G}}_\theta\nabla\theta$, and the second two terms originate from $\tilde{\mathbf{H}}_\theta\nabla L$. To simplify this expression, we note that

$$\nabla^{\mathrm{T}}\tilde{\mathbf{G}}_\theta = -2(\nabla^{\mathrm{T}}\theta)\sin2\theta\mathbf{G} + 2(\nabla^{\mathrm{T}}\theta)\cos2\theta\mathbf{H} = 2(\nabla\theta)^{\mathrm{T}}\tilde{\mathbf{H}}_\theta, \quad \text{and} \tag{38}$$

$$\nabla^{\mathrm{T}}\tilde{\mathbf{H}}_\theta = -2(\nabla^{\mathrm{T}}\theta)\sin2\theta\mathbf{H} - 2(\nabla^{\mathrm{T}}\theta)\cos2\theta\mathbf{G} = -2(\nabla\theta)^{\mathrm{T}}\tilde{\mathbf{G}}_\theta. \tag{39}$$

Inserting these into (37) leads to

$$F = \overbrace{-\mathrm{tr}(\tilde{\mathbf{H}}_\theta\nabla\nabla^{\mathrm{T}})L}^{F_1} + \overbrace{4(\nabla\theta)^{\mathrm{T}}\tilde{\mathbf{G}}_\theta\nabla L}^{F_2} + \overbrace{2L\mathrm{tr}(\tilde{\mathbf{G}}_\theta\nabla\nabla^{\mathrm{T}})\theta}^{F_3} + \overbrace{4L(\nabla\theta)^{\mathrm{T}}\tilde{\mathbf{H}}_\theta\nabla\theta}^{F_4}, \tag{40}$$

with F_3, F_4, and one-half of F_2 originating from $2L\tilde{\mathbf{G}}_\theta\nabla\theta$ and F_1 and the other half of F_2 originating from $\tilde{\mathbf{H}}_\theta\nabla L$. The forms for F_2 and F_4 match those given in (16). To convert the forms of F_1 and F_3 in (40) to those in (16), note that for any constant matrix $\mathbf{C}$,

$$\mathrm{tr}(\mathbf{C}\nabla\nabla^{\mathrm{T}}) = \nabla^{\mathrm{T}}\mathbf{C}\nabla. \tag{41}$$

Applying this to (25)–(26), one finds

$$\mathrm{tr}(\tilde{\mathbf{G}}_\theta\nabla\nabla^{\mathrm{T}}) = \cos2\theta\nabla^{\mathrm{T}}\mathbf{G}\nabla + \sin2\theta\nabla^{\mathrm{T}}\mathbf{H}\nabla, \quad \text{and} \tag{42}$$

$$\mathrm{tr}(\tilde{\mathbf{H}}_\theta\nabla\nabla^{\mathrm{T}}) = \cos2\theta\nabla^{\mathrm{T}}\mathbf{H}\nabla - \sin2\theta\nabla^{\mathrm{T}}\mathbf{G}\nabla, \tag{43}$$

which converts the forms of F_1 and F_3 to those in (16). This verifies that the two-term decomposition of F into two distinct portions $F_\theta \equiv \nabla\cdot\mathbf{f}_\theta$ and $F_L \equiv \nabla\cdot\mathbf{f}_L$, with $\mathbf{f}_\theta$ and $\mathbf{f}_L$ defined as in (12) and (13), respectively, corresponds to $F_L = F_1 + F_2/2$ and $F_\theta = F_2/2 + F_3 + F_4$ with F_1–F_4 given by (32)–(35).

Making use of (42) and (43), and choosing a coordinate system locally aligned with the ellipse, (40) becomes

$$F = \overbrace{-(\tilde{\nabla}^{\mathrm{T}}\mathbf{H}\tilde{\nabla})L}^{F_1} + \overbrace{4(\tilde{\nabla}\theta)^{\mathrm{T}}\mathbf{G}(\tilde{\nabla}L)}^{F_2} + \overbrace{2L(\tilde{\nabla}^{\mathrm{T}}\mathbf{G}\tilde{\nabla})\theta}^{F_3} + \overbrace{4L(\tilde{\nabla}\theta)^{\mathrm{T}}\mathbf{H}(\tilde{\nabla}\theta)}^{F_4}, \tag{44}$$

where $\tilde{\nabla}$ is the gradient matrix in the rotated reference frame. Here, one sees that F_2 and F_4 involve inner products of two gradient vectors modified by the presence of the reflection matrices $\mathbf{G}$ and $\mathbf{H}$, while F_1 and F_3 similarly involve second-order derivatives resembling modified Laplacians. This suggests the operations contributing to F can be understood in terms of generalizations of inner products and Laplacians that involve reflections in the reference frame of the ellipse, a perspective that is explored further in the appendix.

4. An application

To illustrate the geometric decomposition of the eddy forcing, here we use it to analyze eddy–mean flow interactions in a numerical simulation of a quasigeostrophic, barotropically unstable jet on a beta plane that evolves freely from an eastward inflow condition at the western boundary. This system idealizes western boundary current (WBC) jet extensions, such as the Gulf Stream and Kuroshio Extensions, and has been studied extensively in

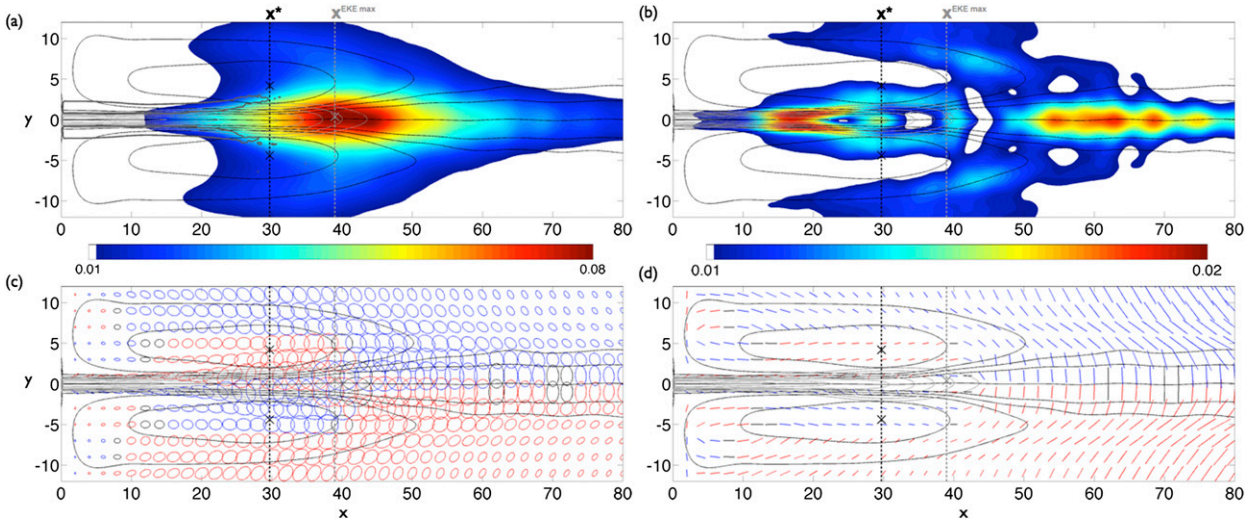

FIG. 3. A summary of the variance ellipse geometry in the idealized western boundary current jet showing (a) the eddy kinetic energy K, (b) the ellipse anisotropy L, (c) the time-mean variance ellipses, and (d) the anisotropic portion of the variance ellipse geometry visualized as line segments with orientation θ and length proportional to $\sqrt{L}$. In (a), the thin gray contour indicates time-mean speed, and the thick gray contour indicates the outer boundary of regions where the meridional gradient of time-mean vorticity is negative. In (c) and (d), ellipses or line segments having positive values of θ (northward tilt with respect to the eastward direction) are shown in red, while those with negative values of θ are shown in blue and those with purely east–west or north–south orientations are shown in black. In all panels, black contours show the time-mean streamfunction, and domain axes are given in nondimensional length units, with one unit corresponding to ~40 km if the inflowing jet is scaled to match the Kuroshio jet at the location of its separation from the coast (see Waterman and Jayne 2011). Two black crosses mark the extrema of the time-mean streamfunction that are found inside time-mean jet-flanking recirculation gyres; these occur at a zonal location $x \sim 30$, denoted x^*, and this is indicated by the black dashed–dotted line. A gray cross marks the maximum of the eddy kinetic energy; this occurs at $x \sim 38$, denoted x^{EKEmax}, and is marked by the gray dashed–dotted line.

Waterman and Jayne (2011) and Waterman and Hoskins (2013). Model details are as in those references.

a. Background

The key properties of the idealized WBC jet system and its time-mean variance ellipse geometry are summarized in Fig. 3. Two important landmarks are the zonal location of the time-mean transport maxima, denoted x^*, and the zonal location of the eddy kinetic energy maximum, denoted x^{EKEmax}. The location x^* has been found to mark the alongstream transition between a potentially unstable and a necessarily stable time-mean jet, under the assumption that one may apply the global necessary condition for barotropic instability to the local time-mean vorticity gradient (Waterman and Jayne 2011). The location x^{EKEmax} occurs downstream from x^* on account of the jet's alongstream advection of growing instabilities.

The ellipse anisotropy L for this system, shown in Fig. 3b, exhibits a very different pattern from the eddy kinetic energy K shown in Fig. 3a. Whereas K has a single broad maximum in the vicinity of x^{EKEmax}, L has two local maxima on the jet flanks in the unstable jet region upstream from x^* and is also elevated downstream from the eddy kinetic energy maximum at x^{EKEmax}. This downstream region, the so-called wave radiator region, has been previously identified as one in which jet meanders induce Rossby wave radiation (Waterman and Jayne 2011; Waterman and Hoskins 2013).

The variance ellipses, shown in Fig. 3c, incorporate information about the relative ellipse size, through K; the ellipse shape, through the ratio L/K; and the ellipse orientation, through θ. Inside the jet in the upstream region where L is large, ellipses are strongly eccentric, with $L/K \approx 1$. Modest eccentricity is seen in the downstream wave radiator region as well. The orientation is more clearly seen via a visualization of the anisotropic component of $\mathbf{C}$ only. Figure 3d displays line segments with length proportional to $\sqrt{L}$ and an orientation angle θ—a representation that ignores the total eddy kinetic energy K, as this is not associated with ellipse orientation. In the region upstream from x^*, the pattern of orientation is seen to be consistent with barotropic instability, with variance ellipses (and line segments) tilted into the jet shear to extract energy from the mean flow. Downstream from x^{EKEmax}, ellipse orientation shows a westward-facing "horseshoe" pattern characteristic of the tilt of Rossby wave phase lines.

Based on analysis of previous studies (e.g., Waterman et al. 2011; Waterman and Hoskins 2013), we understand that the eddy forcing in this model is a result of eddies acting to redistribute the strong positive and negative vorticity anomalies in the northern and southern half

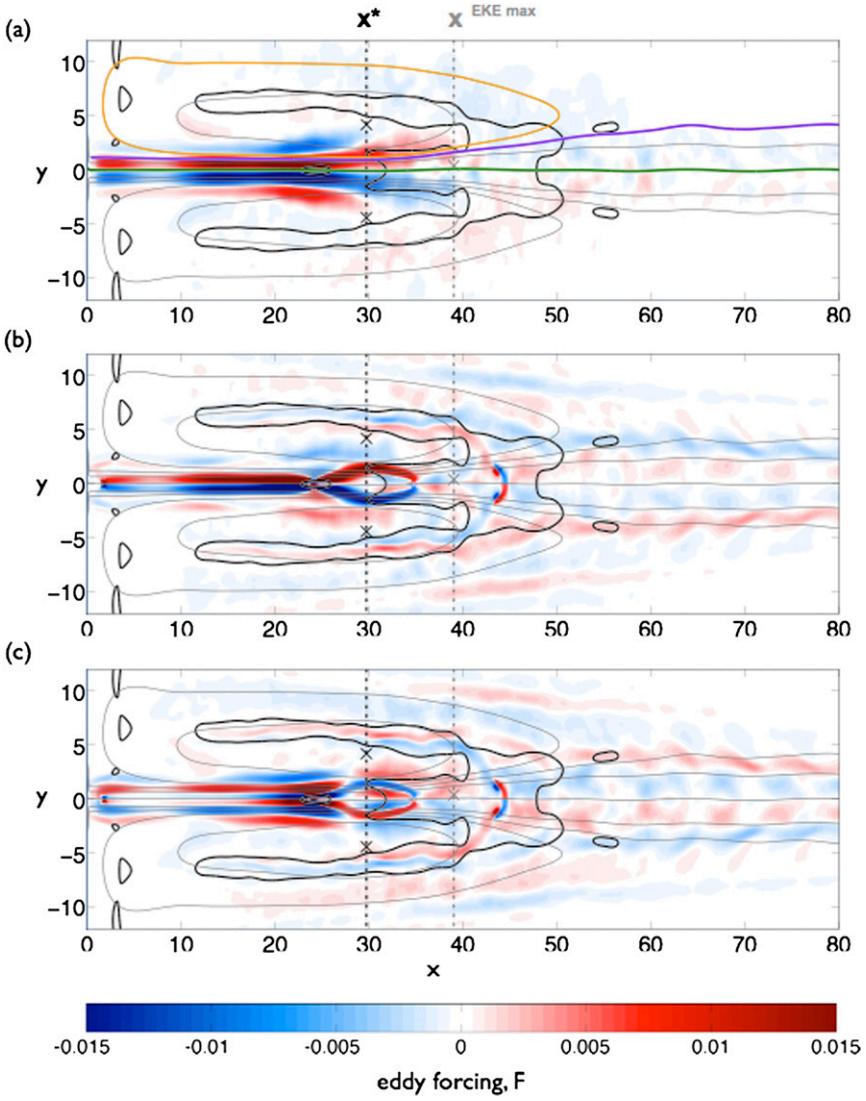

FIG. 4. (a)The total eddy forcing F in the idealized western boundary current jet, (b) together with the contribution F_θ arising from variations in ellipse orientation θ, and (c) the contribution F_L arising from variations in ellipse anisotropy L. The vertical lines, crosses, and contours of the time-mean streamlines (now shown in gray) are all as described in Fig. 3. Black contours now outline regions of the eddy anisotropy parameter $L/K < 0.1$. In such regions, the variance ellipses are nearly circular, and the geometric decomposition is not well defined, as described in the text. The colored contours in (a) denote three boundaries for which cross-contour fluxes are computed: the jet axis (green); the northern jet boundary (purple), defined as the outermost streamline intersecting the eastern boundary; and the northern recirculation (yellow), defined as the outermost closed streamline.

jets, respectively, associated with the unstable jet's shear. Upstream from x^{EKEmax}, eddies flux vorticity down the background vorticity gradient, in this way acting to stabilize the jet against barotropic instability and drive the time-mean recirculations. Downstream from x^{EKEmax}, the divergent part of the eddy vorticity flux is up the background gradient and acts to strengthen or maintain the jet. The eddy forcing results from the net vorticity convergences and divergences that result from these flux patterns.

The total eddy forcing F is presented in Fig. 4a and is best described in terms of three distinct alongstream regions, as follows:

(i) An upstream unstable jet, $x < x^*$. In this region, the divergent part of the eddy vorticity flux $\langle \mathbf{u}'\zeta' \rangle$

is down the vorticity gradient of the unstable time-mean jet. Given that here the time-mean jet has regions of negative vorticity gradient on its flanks (Fig. 3a), this results in a quadrupole pattern of vorticity flux convergences and divergences. The eddy forcing F is dominated by strong vorticity flux divergence (positive F) inside the northern jet core and strong vorticity flux convergence (negative F) on the northern jet flank, together with the reverse pattern in the southern half jet. This quadrupole of F forces an eddy-driven circulation that decelerates the jet at its core and accelerates it on its flanks, in this way acting to reduce the jet's large-scale meridional shear and stabilize its barotropic instability. Furthermore this pattern accounts for the net eddy flux of vorticity from the jet into the flanking recirculation gyres.

(ii) A transition region, $x^* < x < x^{\mathrm{EKEmax}}$. Here, $\langle \mathbf{u}'\zeta' \rangle$ continues to be down the time-mean vorticity gradient, which no longer exhibits a sign reversal on the jet flanks on account of the jet's stabilization in the upstream region. The F quadrupole pattern of the upstream region becomes a dipole pattern, with a divergence (positive F) in the northern half jet and a convergence (negative F) in the southern half jet. Eddies continue to decelerate the jet core, but now also act to weaken the flow on the jet flanks and to close the recirculation gyres. In this region, the time-mean jet no longer satisfies the necessary condition for instability, but the time-mean eddy kinetic energy continues to grow with along-jet distance as perturbations are swept downstream.

(iii) A downstream wave radiator region, $x > x^{\mathrm{EKEmax}}$. In this region, $\langle \mathbf{u}'\zeta' \rangle$ becomes upgradient, with a weak convergence in the northern half jet and a weak divergence in the southern half jet. This is permitted by a convergence in eddy enstrophy (not shown) as eddy energy decays with along-jet distance. The eddy forcing, known to originate in Rossby wave radiation from the meandering jet, acts to maintain the time-mean jet strength downstream by weakly accelerating it.

More details on these aspects of the flow and the eddy–mean flow forcing can be found in Waterman and Jayne (2011) and Waterman and Hoskins (2013). Next we turn to applying the geometric decomposition to this system to see what it can add to our understanding.

b. Geometric decomposition of the eddy forcing

A geometric decomposition of the eddy forcing in this zonally evolving jet system will be considered from multiple perspectives. First, we will examine the second-order spatial variations of F_L and F_θ presented in Fig. 4. Second, the linear variations of the flux vectors $\mathbf{f}_L$ and $\mathbf{f}_\theta$ will be examined along key regional boundaries presented in Fig. 5. Finally, for a more quantitative description, we will average divergence and flux vector quantities over strategically defined regions and regional boundaries respectively, as summarized in Fig. 6. Each of these approaches describes the same eddy forcing as well as the same breakdown into contributions from ellipse orientation and ellipse anisotropy but does so from a unique perspective with different merits.

The decomposition of F into F_L and F_θ (Figs. 4b,c) reveals the following features of note:

- In the upstream region inside the jet, F_θ dominates the total eddy forcing. Thus, we can attribute the weakening of the jet core, and the resulting eddy stabilization of the time-mean jet, to changing ellipse orientation inside the jet as it evolves downstream.
- On the jet flanks and recirculation edges upstream from x^*, the eddy forcing is primarily associated with F_L; the pattern of significant F_θ in this region is narrowly confined to the jet core. Given that this pattern of F_L accomplishes a deposit of positive vorticity from the northern jet flank into the northern recirculation gyre and negative vorticity from the southern jet flank into the southern recirculation gyre, we can attribute the eddy driving of the recirculations to the spatial patterns of ellipse anisotropy on the jet flanks and jet-flanking edges of the recirculations.
- In the downstream region with $x > x^{\mathrm{EKEmax}}$, both F_θ and F_L are significant inside the broadened time-mean jet, where they make oppositely signed contributions in alternating bands. Hence, we can attribute the eddy strengthening of the downstream jet to the spatial patterns of both ellipse orientation and ellipse anisotropy inside the downstream jet.

Another feature of note is the significant cancellation between F_L and F_θ that occurs in a circular region near the EKE maximum and in a backward C-shaped halo extending westward into the recirculation gyres. These cancelling patterns are predominantly observed in regions in which the ratio L/K is small, and therefore the variance ellipses are nearly circular. In such instances, our geometric decomposition becomes ill defined because the orientation angle of a circle is not defined. We know that when variance ellipses are nearly circular, the resulting eddy fluxes must be small, but in this case the geometric decomposition can lead to orientation angles that fluctuate rapidly. The cancelling patterns of F_L and F_θ within the region for which $L/K < 0.1$, given by the

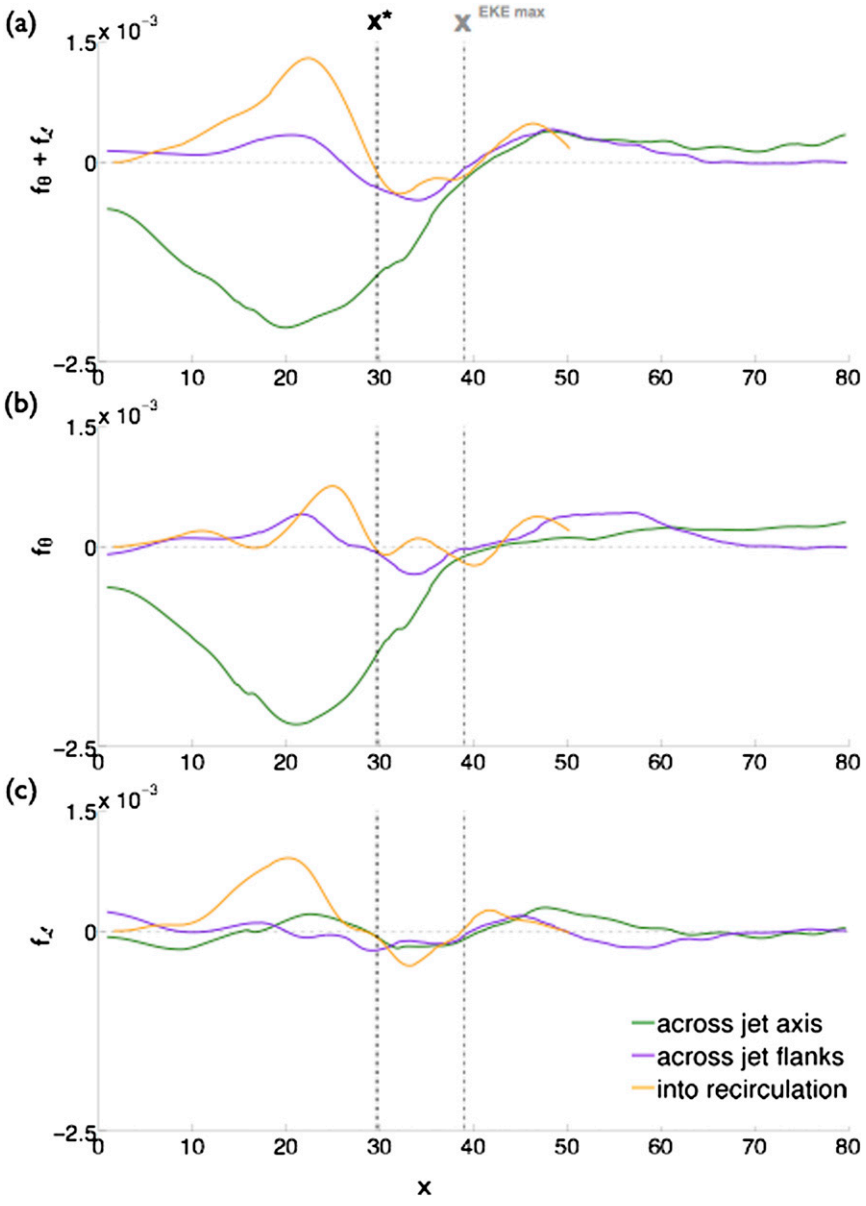

FIG. 5. Along-jet sections of the portion of **f**—the divergent part of the eddy vorticity flux—and its geometric components $\mathbf{f}_L$ and $\mathbf{f}_\theta$, normal to the bounding curves of key regions. The normal flux $\mathbf{f} \cdot \hat{\mathbf{n}}$ is shown in (a), while the normal fluxes $\mathbf{f}_\theta \cdot \hat{\mathbf{n}}$ and $\mathbf{f}_L \cdot \hat{\mathbf{n}}$ are shown in (b) and (c); here, $\hat{\mathbf{n}}$ is the unit normal to a particular curve. In each panel, the three lines show the normal flux across the time-mean jet axis near $y = 0$ (green), the time-mean jet's northern boundary (purple), and the southern boundary of the northern time-mean recirculation gyre (yellow); streamlines defining these boundaries are highlighted by thick colored lines in Fig. 4a. Positive values indicate a northward flux of positive vorticity anomaly, or equivalently, a southward flux of negative vorticity anomaly. Curves are smoothed using a running mean with a width of 10 nondimensional length units to emphasize the larger-scale features.

black contours in each panel of Fig. 4, are therefore regarded as spurious. Referring to Figs. 3a and 3b, we find that this happens in regions in which L itself is small, and therefore we should expect small contributions to the eddy forcing F because all the terms in F involve L or its derivatives. The fact that the eddy kinetic energy K is large in this region is not a concern because spatial variations in K do not contribute to F.

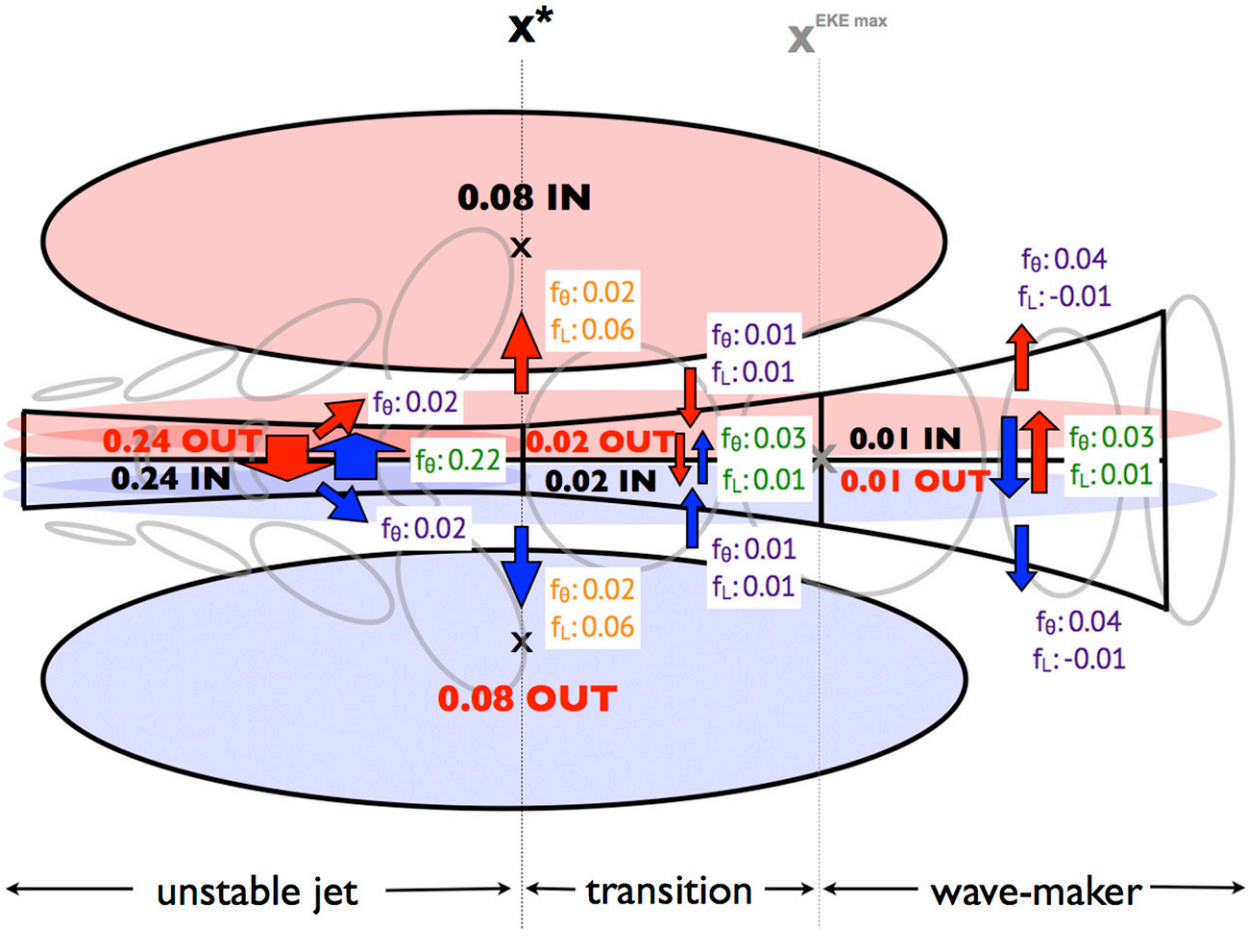

FIG. 6. A schematic summarizing an integral view of the eddy forcing and its breakdown into components arising from the spatial variations of L and θ. We divide the system into eight regions: two recirculations, defined by the outermost closed streamlines (with the yellow curve in Fig. 4a indicating the northern recirculation), and six alongstream regions within the jet core. The six jet core regions correspond to the northern and southern halves of the unstable jet region, transition region, and wave radiator region described in the text. They are bounded meridionally by the jet boundaries (with the purple curve in Fig. 4a indicating the northern jet boundary) and the jet axis (the green curve in Fig. 4a) and zonally by the western boundary, $x = x^*$, $x = x^{\mathrm{EKEmax}}$, and the eastern boundary. The background color indicates regions of significant background positive (red) or negative (blue) vorticity anomaly associated with the time-mean jet and recirculation gyres. Gray ellipses are a simplified schematic representation of the along-jet evolution of eddy shape and orientation. We compute the area integral of the total eddy vorticity flux divergence inside each region, indicated by the red and black bold numbers in nondimensional units, with black font indicating a net vorticity flux convergence and red font indicating a net vorticity flux divergence. The net flux of $\mathbf{f}$ across the boundary of each region is also computed, as well as its breakdown into $\mathbf{f}_L$ and $\mathbf{f}_\theta$ components, with scaled arrows indicating the total flux. The arrows point in the direction of the net flux across the boundary, while the color indicates whether the flux is of a positive vorticity anomaly (red) or a negative vorticity anomaly (blue); the pairs of red and blue arrows near the jet axis indicate that these can either be interpreted as fluxes of positive vorticity or as fluxes of negative vorticity in the opposite direction. The colored numbers beside each arrow or set of arrows indicate the magnitude of the flux in the $\mathbf{f}_L$ and $\mathbf{f}_\theta$ components, respectively, in nondimensional units of integrated vorticity flux. Note that the fluxes across the four meridional boundaries inside the jet are an order of magnitude smaller than those across the jet core and jet edges; for simplicity, these numbers are not shown.

The divergent part of the eddy vorticity flux $\mathbf{f}$ is decomposed into the contributions $\mathbf{f}_L$ and $\mathbf{f}_\theta$ along key regional boundaries, as presented in Fig. 5. The three boundaries chosen are the jet axis (green), the northern jet edge (purple), and the edge of the northern recirculation gyre (yellow); these are indicated in Fig. 4a. Consistent with the spatial patterns of F_L and F_θ, the decomposition of the flux vector reveals the following: (i) $\mathbf{f}_\theta$ overwhelmingly dominates the total divergent eddy vorticity flux across the jet axis upstream from x^*; (ii) $\mathbf{f}_L$ accounts for the bulk of the divergent eddy vorticity flux into the recirculations upstream from x^*, but variations in θ along the jet-flanking boundary of the recirculation gyres also play a nonnegligible role; and (iii) both $\mathbf{f}_L$ and $\mathbf{f}_\theta$ play an important role in determining the total eddy flux both across the jet axis and across the jet flanks in the downstream region. On the jet axis $\mathbf{f}_\theta$ and $\mathbf{f}_L$ tend to contribute to the total flux in the same

sense, whereas on the jet flanks $\mathbf{f}_\theta$ and $\mathbf{f}_L$ tend to make opposing contributions.

A consolidated view of the eddy forcing in the system is perhaps best viewed and summarized via the calculation of the net eddy forcing and/or the net divergent eddy vorticity flux—along with their geometric decompositions—inside and/or across key regions or regional boundaries of the system (Fig. 6). This allows a quantitative description of the features identified above. As the model units are nondimensional, numbers are given in units of nondimensional integrated vorticity flux. We find the following:

- In the upstream region inside the jet, with $x < x^*$, the eddy forcing consists of a very large net downgradient eddy vorticity flux of 0.22 across the jet axis as well as a much more modest downgradient flux of 0.02 across the jet flanks. Together these result in a very large net eddy vorticity flux divergence of 0.24 in the northern half jet and a similar convergence in the southern half jet. This cross-jet flux in the upstream region is the largest eddy flux in the domain by an order of magnitude, and the resulting flux convergence/divergence is the dominant term in the time-mean vorticity balance in the region. It is accomplished entirely by variations in θ along the region boundaries and primarily by fluxes of $\mathbf{f}_\theta$ across the jet axis.
- For the recirculation gyres, we find an integrated eddy flux of positive vorticity of 0.08 into the northern recirculation gyre and a comparable flux of negative vorticity into the southern recirculation gyre. The geometric decomposition shows that ~75% of this eddy forcing is accounted for by variations of ellipse anisotropy along the recirculation edge, although eddy forcing derived from the variations in ellipse orientation makes a nonnegligible contribution, accounting for ~25% of the total forcing.
- In the downstream wavemaker region, more modest upgradient fluxes of 0.04 and 0.03 are seen across the jet axis and jet edges, respectively. This results in a small net eddy vorticity flux convergence of 0.01 in the northern half jet and a similar divergence in the southern half jet. The geometric decomposition shows that this eddy forcing is described by a combination of contributions from θ and L. Across the jet axis, eddy forcing from variations in ellipse orientation and anisotropy act in the same sense, while across the jet edges, they counteract each other's effects, with a dominance of θ variations in both cases.

c. Summary

Taken all together, the consideration of the eddy forcing in this system from the perspective of the geometric decomposition has illustrated that the dominant eddy forcing in the system is a stabilization of the unstable jet upstream from $x = x^*$, achieved via an eddy vorticity flux across the jet axis due almost entirely to variations of the ellipse orientation. This is consistent with a growing barotropic instability with alongstream distance to x^*, with ellipses along the jet axis tilting more and more into the shear of the jet. A flux of vorticity away from the jet core and to the jet flanks, also associated with the variation of ellipse orientation, also contributes to jet stabilization, although this accounts for only 0.02/0.24 or ~10% of the total eddy redistribution of the jet's vorticity anomaly.

This new view of the eddy forcing has also given insight into the divergent part of the eddy vorticity flux between the jet and the time-mean recirculation gyres. We find that the eddy vorticity flux into the gyres is primarily associated with variations of ellipse anisotropy L between the jet flanks and the gyres' jet-flanking edge in the region upstream from $x = x^*$. This is the same region in which the anisotropy L exhibits a maximum on the jet flanks, as seen in Fig. 3b. In addition, we have seen that the net upgradient eddy flux in the wave radiator region responsible for the eddy strengthening of the jet downstream is largely accomplished by variations in ellipse orientation along the jet axis and jet edges, although variations in ellipse anisotropy also does play a role.

Finally, the transition region $x^* < x < x^{\mathrm{EKEmax}}$ emerges as a region where the geometric decomposition appears to provide little insight. Here, the total eddy vorticity flux tends to be much more equally split between the two geometric terms, and there exist patterns of strong cancellation in F_θ and F_L, with almost no expression in the total F. As mentioned above, these canceling patterns predominantly occur in regions in which the ratio L/K is small, and therefore the variance ellipses are nearly circular. The contour $L/K = 0.1$ appears to be a cutoff here below which the geometric composition does not yield useful information, although the rationale behind this cutoff value merits closer investigation. Results at this stage indicate that we should interpret the geometric decomposition cautiously in regions where the variance ellipses are nearly circular.

5. Discussion

In this paper, we have introduced a new framework that describes eddy–mean flow feedback effects in terms of the spatial patterns of variance ellipse geometry. Specifically, we have shown that the eddy vorticity flux convergence F can be decomposed into four distinct geometric terms: one arising only from spatial variations in the ellipse anisotropy L, two arising only from variations in ellipse orientation θ, and a cross term that depends upon both L and θ. Application of the divergence

theorem leads to a simpler decomposition of F into two terms, with the integral value of F over a region controlled by separate variations in the anisotropy L and the orientation θ around the region periphery. These geometric decompositions emerge from the realization that the velocity covariance matrix, from which one may compute F, itself has a geometric interpretation in terms of the variance ellipses.

Application of this framework to the description of eddy–mean flow feedbacks in an idealized western boundary current jet reveals that while spatial patterns of L and θ are locally important in different regions, in general, variations in θ are more important in fluxing vorticity across key boundaries within the jet, while vorticity fluxes from variations in L dominate in driving the recirculations. The physical reasons for these results are not yet known. It is reasonable to hypothesize that the partitioning of fluxes between L and θ variations reflects the nature of the physical process driving the eddy forcing, in which case the geometric decompositions derived here could provide clues to the underlying dynamics. Investigation of this hypothesis in a variety of flow configurations is a topic for future work. In particular, an intriguing question is whether the dominance of θ variations across jet boundaries, and of L variations across recirculation boundaries, is a general result.

For reasons of simplicity, here we have limited this work to the consideration of the velocity covariance matrix in the two-dimensional (barotropic) case, and its implications for eddy–mean flow interactions under the quasigeostrophic approximation. Eddy forcing can also be examined in the three-dimensional case with the hydrostatic Boussinesq Navier–Stokes equations; see Maddison and Marshall (2013) for a discussion. A key task ahead is to extend the geometric decomposition framework to the three-dimensional case by including eddy fluxes of buoyancy in addition to the horizontal fluxes of horizontal momentum. The geometric aspects are more complicated in this case because the two-dimensional ellipse described here is replaced by a three-dimensional ellipsoid.

The decompositions presented here directly link eddy mean–flow forcing to specific arrangements of variance ellipse geometry. The ability to identify the patterns of ellipse geometry that give rise to a mean flow forcing has the potential to simplify descriptions of eddy–mean flow interactions and perhaps to suggest new ideas for the task of eddy parameterization. For example, we have shown that there are 30 possible ways that ellipse geometry can present second-order spatial variations, but only the four specific patterns we have identified here contribute to eddy forcing of the mean flow. A particularly compelling direction for future work is to determine whether specific physical mechanisms may be definitively associated with different terms in the geometric decomposition. The search for parameterizations based on properties of eddy geometry has been the subject of the recent works by Marshall et al. (2012) and Maddison and Marshall (2013), and we see the present effort as offering a promising contribution to this direction.

Acknowledgments. SW acknowledges the support of Grants RM10240 and CE110001028 from the Australian Research Council. The work of JML was supported by Award 1235310 from the Physical Oceanography program of the United States National Science Foundation.

APPENDIX

Second-Order Ellipse Quantities

Here, we ask, in principle, how many second-order ellipse quantities could potentially contribute to F_1–F_4. There are two types of second-order spatial rates of change arising from K, L, and θ: second-order partial derivatives and products of two first-order partial derivatives. There are $3 \times 3 = 9$ second-order derivatives, corresponding to $\partial^2/\partial x^2$, $\partial^2/\partial y^2$, and $\partial^2/(\partial x \partial y)$ of K, L, and θ, respectively. Of these, only two combinations—representing F_1 and F_3—appear in the eddy vorticity flux divergence. From the three ellipse quantities, there are six first-order spatial rates of change, corresponding to $\partial/\partial x$ and $\partial/\partial y$. There are then 21 different products of any two of these six quantities, which is the same as the number of off-diagonal elements in a 6×6 matrix (15 terms) plus the number of diagonal elements (6 terms). Of these, only two combinations—representing F_2 and F_4—appear in the eddy vorticity flux divergence. Thus, of the 30 possible second-order terms, only 4 contribute to the eddy forcing.

Examining the possible derivative terms in further detail will shed light on the terms that contribute to the eddy forcing. Here, we let the matrix $\mathbf{J}$ with no input argument be the 90° counterclockwise rotation matrix:

$$\mathbf{J} = \begin{bmatrix} 0 & -1 \\ 1 & 0 \end{bmatrix}. \tag{A1}$$

Using the four matrices $\mathbf{I}$, $\mathbf{J}$, $\mathbf{G}$, and $\mathbf{H}$, we may then define four generalized inner products between a pair of two vectors $\mathbf{f}$ and $\mathbf{g}$ as

TABLE A1. Nine possible second-order derivatives of the three ellipse quantities, with the locations of the terms contributing to F_1 and F_3 marked.

	$\nabla^T\mathbf{I}\nabla$	$\nabla^T\mathbf{J}\nabla$	$\nabla^T\mathbf{G}\nabla$	$\nabla^T\mathbf{H}\nabla$
K	·	0	·	·
L	·	0	·	F_1
θ	·	0	F_3	·

$$\mathbf{f}\cdot\mathbf{g}\mapsto\mathbf{f}^T\mathbf{I}\mathbf{g}=f_xg_x+f_yg_y, \tag{A2}$$

$$-\mathbf{k}\cdot\mathbf{f}\times\mathbf{g}\mapsto\mathbf{f}^T\mathbf{J}\mathbf{g}=f_yg_x-f_xg_y, \tag{A3}$$

$$\mathbf{f}^T\mathbf{G}\mathbf{g}=f_xg_x-f_yg_y, \quad \text{and} \tag{A4}$$

$$\mathbf{f}^T\mathbf{H}\mathbf{g}=f_xg_y+f_yg_x, \tag{A5}$$

where the first is the standard inner product, and the second is the negative of the cross product; this is indicated at the left in conventional notation, in which $\mathbf{f}$ and $\mathbf{g}$ are interpreted as three-vectors.

The third and fourth inner products do not appear to have standard names but are reflectional vector products representing the inner product between one vector and another that has been subjected to a reflection, just as the cross product in two dimensions represents an inner product between one vector and another that has been rotated 90°. Note that of these four inner products, one vanishes identically if $\mathbf{f}=\mathbf{g}$ and that is the cross-product version $\mathbf{f}^T\mathbf{J}\mathbf{f}=0$.

These matrices can be used to construct the generalized Laplacians $\nabla^T\mathbf{I}\nabla$, $\nabla^T\mathbf{J}\nabla$, $\nabla^T\mathbf{G}\nabla$, and $\nabla^T\mathbf{H}\nabla$. However, $\nabla^T\mathbf{J}\nabla$ is found to vanish identically. The operators $\nabla^T\mathbf{G}\nabla$ and $\nabla^T\mathbf{H}\nabla$ could be termed reflectional Laplacians by analogy with the horizontal Laplacian ∇^2, given by $\nabla^T\mathbf{I}\nabla=\nabla^T\nabla$. It is evident that $\nabla^T\mathbf{I}\nabla$, $\nabla^T\mathbf{G}\nabla$, and $\nabla^T\mathbf{H}\nabla$ together form a complete set of second-order derivatives because they are a rearrangement of the three partial derivatives $\partial^2/\partial x^2$, $\partial^2/\partial y^2$, and $\partial^2/(\partial x\partial y)$.

We can now examine the possible second-order spatial rates of change arising from K, L, and θ, with respect to these groupings. Second-order partial derivatives are shown in Table A1, while products of two first-order partial derivatives are shown in Table A2. This shows all 30 of the terms discussed above—not counting those that are identically zero—with the locations of F_1–F_4 marked. One sees more clearly the possible second-order derivatives and generalized inner products, in particular, the nature of the 26 nonzero terms that do not contribute to the eddy forcing.

TABLE A2. The 21 possible second-order products of first-order derivatives of the three ellipse quantities, with the locations of the terms contributing to F_2 and F_4 marked.

	$[\nabla f]^T\mathbf{I}[\nabla g]$			$[\nabla f]^T\mathbf{J}[\nabla g]$			$[\nabla f]^T\mathbf{G}[\nabla g]$			$[\nabla f]^T\mathbf{H}[\nabla g]$		
	K	L	θ	K	L	θ	K	L	θ	K	L	θ
K	·	·	·	0	·	·	·	·	·	·	·	·
L		·	·		0	·		·	F_2		·	·
θ			·			0			·			F_4

REFERENCES

Cronin, M., 1996: Eddy–mean flow interaction in the Gulf Stream at 68°W. Part II: Eddy forcing on the time-mean flow. *J. Phys. Oceanogr.,* **26,** 2132–2151, doi:10.1175/1520-0485(1996)026<2132:EMFIIT>2.0.CO;2.

Gent, P. R., and L. C. McWilliams, 1996: Eliassen–Palm fluxes and the momentum equation in non-eddy-resolving ocean models. *J. Phys. Oceanogr.,* **26,** 2539–2546, doi:10.1175/1520-0485(1996)026<2539:EFATME>2.0.CO;2.

Holland, W. R., and P. B. Rhines, 1980: An example of eddy induced ocean circulation. *J. Phys. Oceanogr.,* **10,** 1010–1031, doi:10.1175/1520-0485(1980)010<1010:AEOEIO>2.0.CO;2.

Hoskins, B. J., 1983: Modelling of transient eddies and their feedback on the mean flow. *Large-Scale Dynamical Processes in the Atmosphere,* B. J. Hoskins and R. P. Pearce, Eds., Academic Press, 169–199.

——, I. N. James, and G. H. White, 1983: The shape, propagation and mean-flow interaction of large-scale weather systems. *J. Atmos. Sci.,* **40,** 1595–1612, doi:10.1175/1520-0469(1983)040<1595:TSPAMF>2.0.CO;2.

Lumpkin, R., and G. C. Johnson, 2013: Global ocean surface velocities from drifters: Mean, variance, El Niño–Southern Oscillation response, and seasonal cycle. *J. Geophys. Res. Oceans,* **118,** 2992–3006, doi:10.1002/jgrc.20210.

Maddison, J. R., and D. P. Marshall, 2013: The Eliassen–Palm flux tensor. *J. Fluid Mech.,* **729,** 69–102, doi:10.1017/jfm.2013.259.

Marshall, D. P., J. R. Maddison, and P. S. Berloff, 2012: A framework for parameterizing eddy potential vorticity fluxes. *J. Phys. Oceanogr.,* **42,** 539–557, doi:10.1175/JPO-D-11-048.1.

Marshall, J. C., 1984: Eddy-mean-flow interaction in a barotropic ocean model. *Quart. J. Roy. Meteor. Soc.,* **110,** 573–590, doi:10.1002/qj.49711046502.

Morrow, R., R. Coleman, J. Church, and D. Chelton, 1994: Surface eddy momentum flux and velocity variances in the Southern Ocean from Geosat altimetry. *J. Phys. Oceanogr.,* **24,** 2050–2071, doi:10.1175/1520-0485(1994)024<2050:SEMFAV>2.0.CO;2.

Ohlmann, J. C., and P. P. Niiler, 2005: Circulation over the continental shelf in the northern Gulf of Mexico. *Prog. Oceanogr.,* **64,** 45–81, doi:10.1016/j.pocean.2005.02.001.

Plumb, R. A., 1986: Three-dimensional propagation of transient quasi-geostrophic eddies and its relationship with the eddy forcing of the time–mean flow. *J. Atmos. Sci.,* **43,** 1657–1678, doi:10.1175/1520-0469(1986)043<1657:TDPOTQ>2.0.CO;2.

Preisendorfer, R. W., 1988: *Principal Component Analysis in Meteorology and Oceanography.* Elsevier, 425 pp.

Scott, R. B., B. K. Arbic, C. L. Holland, A. Sen, and B. Qiu, 2008: Zonal versus meridional velocity variance in satellite

observations and realistic and idealized ocean circulation models. *Ocean Modell.,* **23,** 102–112, doi:10.1016/j.ocemod.2008.04.009.

Trani, M., P. Falco, and E. Zambianchi, 2011: Near-surface eddy dynamics in the Southern Ocean. *Polar Res.,* **23,** 11 203, doi:10.3402/polar.v30i0.11203.

Waterman, S., and S. R. Jayne, 2011: Eddy-mean flow interactions in the along-stream development of a western boundary current jet: An idealized model study. *J. Phys. Oceanogr.,* **41,** 682–707, doi:10.1175/2010JPO4477.1.

——, and B. J. Hoskins, 2013: Eddy shape, orientation, propagation, and mean flow feedback in western boundary current jets. *J. Phys. Oceanogr.,* **43,** 1666–1690, doi:10.1175/JPO-D-12-0152.1.

——, N. G. Hogg, and S. R. Jayne, 2011: Eddy–mean flow interaction in the Kuroshio Extension region. *J. Phys. Oceanogr.,* **41,** 1182–1208, doi:10.1175/2010JPO4564.1.

Young, W. R., 2012: An exact thickness-weighted average formulation of the Boussinesq equations. *J. Phys. Oceanogr.,* **42,** 692–707, doi:10.1175/JPO-D-11-0102.1.